

Dynamics of low-energy helium vapor pulses

A. Wynveen, K. A. Lidke, M. C. Williams, C. F. Giese, and J. W. Halley
School of Physics and Astronomy, University of Minnesota, Minneapolis, Minnesota 55455
 (Received 3 July 2002; published 19 February 2003)

We report results of experiments in which pulses of helium vapor are produced by a current pulse in a chromium film covered with superfluid helium at around 0.3 K. The pulses were detected by a titanium bolometer operating at 0.47 K. The shape of the detected signal is a strong function of the power of the initiating current pulse. For low powers the signal from a single current pulse also contains a single peak, but for higher powers, a single current pulse produces two and then at the highest powers, three peak signals. To analyze the origin of these phenomena we report results of hybrid gas-dynamics and hydrodynamics simulations, which demonstrate that the signals arise from shock waves formed in the vapor. The shock waves form due to the presence of a gradient in the small ambient background of helium vapor in the chamber and are extremely sensitive to the pulse power.

DOI: 10.1103/PhysRevE.67.026311

PACS number(s): 47.40.Nm, 47.45.-n

I. INTRODUCTION

We are engaged in a program to test the proposal [1,2] that Bose-Einstein condensation in superfluid helium permits anomalously fast reemission of atomic helium particles incident on the superfluid surface, at superfluid surfaces far from the point of impact of the incident particles. Others [3] have carried out experiments in which the superfluid is moving in the laboratory and the atomic helium vapor is stationary. Here, we report experimental detection and characterization of vapor pulses in the apparatus in which the transmission experiment will be carried out. A similar apparatus was used by Silvera and co-workers [4,5] to obtain an estimate of the helium-helium scattering cross section at low energies. Mulders and Wyatt [6] have carried out experiments similar to those reported here and have observed some multipeak structures in the response which are similar to those which we report [7].

In the experiments, we observe multipeak structures at the higher pulse powers available to us. In this paper, we attribute these multipeak structures to the formation of shock waves in the gas. To substantiate this attribution, we present results of hybrid gas-dynamic and hydrodynamic simulations, in which atomically specific gas-dynamics calculations are used to provide initial and boundary conditions for a hydrodynamics calculation. Though some work [8–10] has appeared in which the determination of hydrodynamic boundary conditions from atomic scale simulation was considered or carried out, our approach is somewhat different and we have accordingly described it in some detail.

The next section describes the experiments, the following two sections describe the gasdynamics and hybrid calculations and the final section presents a discussion and conclusions.

II. EXPERIMENTS

We show a diagram of the cell in which the atomic pulsed beams have been made and detected in Fig. 1. The cell resides in a dilution refrigerator and the experiments are carried out at ambient temperatures of 0.3 K. Helium beams are

created by evaporation from the adsorbed film on small resistive elements consisting of a thin film of chromium on sapphire. Current pulses heat the chromium film and thereby the sapphire and helium, evaporating atoms which are then detected using superconducting thin film bolometers.

The temperature resistance characteristic for one of our titanium bolometers is shown in Fig. 2. The bolometers consist of 400 Å of titanium sputter-deposited onto 2.5-mm diameter, 0.2-mm-thick sapphire substrates. They are in weak thermal contact with the cell and thus can be held in the middle of their transition by a feedback circuit [11]. The feedback voltage of the bolometer circuit is amplified and measured with a digital oscilloscope to determine the energy imparted to the detector. We find that these bolometers have

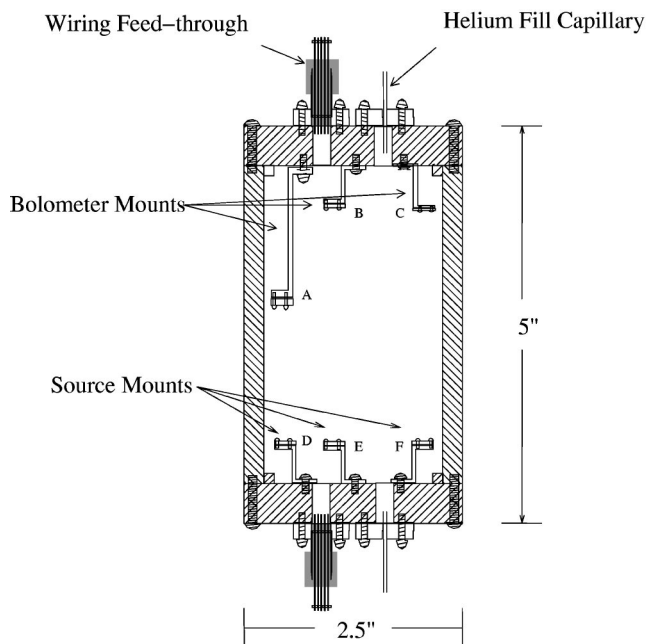
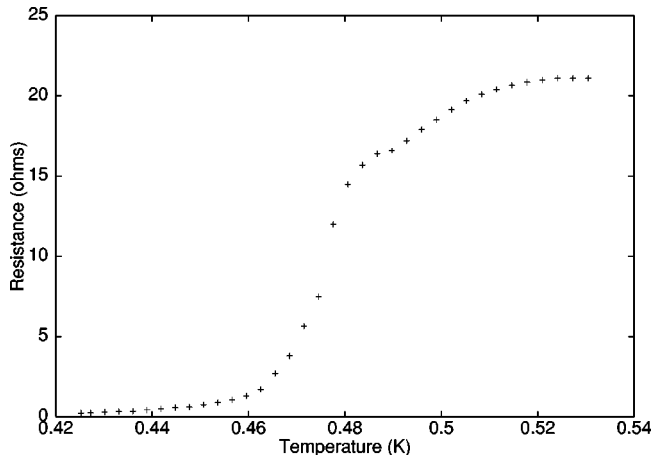


FIG. 1. Experimental cell used in the dilution refrigerator for vapor propagation experiments in the absence of a suspended film. The data reported in this paper were obtained with source *E* and bolometer *B*.

FIG. 2. R versus T for a titanium bolometer.

a rise time of the order of $1 \mu\text{s}$ and a recovery time of the order of ten's of μs . This is consistent with other reported work [12]. Since the bolometers are covered with a thin film of superfluid and the sticking coefficient of helium atoms incident upon the liquid film is nearly unity, each atom in the helium beam is assumed to give up its energy, which is equal to the atom's kinetic energy plus the chemical potential, to the detector.

We show detected pulses in Figs. 3 – 6 in order of increasing pulse power. To maximize the bolometer response, we adjusted the feedback circuit at each pulse power to reset the bolometer at the titanium film superconducting transition temperature. Because of this adjustment, absolute relative intensities between one pulse power and another were not obtained and the experimental data in the figures has been renormalized to make the maximum amplitude 1 in each dataset. In these experiments 256 averages were performed by the oscilloscope to increase the signal to noise ratio. However, the shape of the detected pulses could be clearly seen with a single-source pulse. The simulation data in each figure are discussed in the following sections. In each case, the exciting current pulse in the source was of the form $I(t) = \text{const} \times t^{0.7}$. In particular, there was only one maximum, at

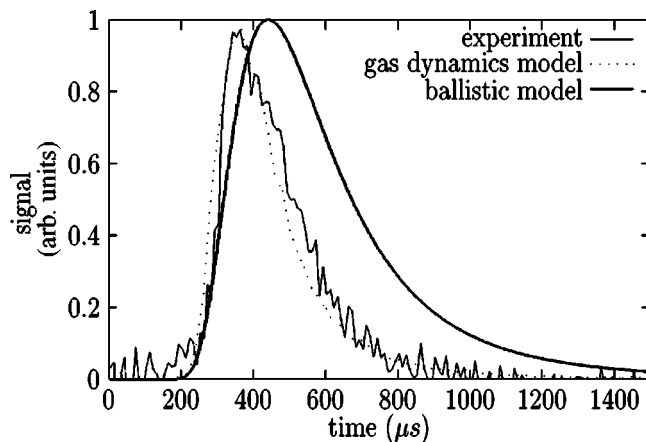


FIG. 3. Detected low power vapor pulse signal compared with simulations.

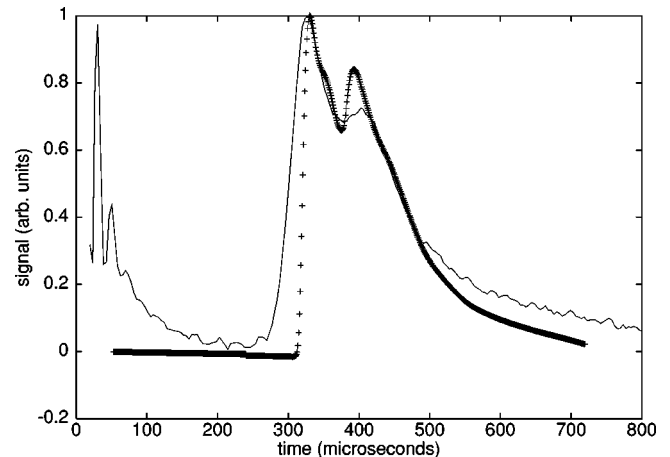


FIG. 4. Detected experimental signal (solid line) for a 4-mW pulse compared to hybrid simulation (+).

the end of the pulse, in the pulse as a function of time. For low power pulses, the detected signal also had just one maximum, but for higher power pulses ($>3 \text{ mW}$), we unexpectedly observed multiple peaks in the detected signals.

We explored a variety of hypotheses in attempts to explain these multiple peaks. We ruled out [13] the possibility that the quasiparticle spectrum of superfluid helium caused the peaks during the evaporation of the vapor pulse because (1) under most circumstances, such effects are not expected in the velocity distribution of excited atoms because of a cancellation of two factors of the quasiparticle density of states in the expression for the current of evaporated particles [14], (2) such effects would not be expected to arise only at high pulse powers, and (3) collisions would be anticipated to damp out any sharp features of the spectrum as the pulse propagates.

We also believe that these multiple peaks did not result from repeated evaporations of the adsorbed helium from the source, which would arise from successive burn off and flow of the superfluid back onto the source. The rapid flow of the superfluid onto the source and the large detected time differ-

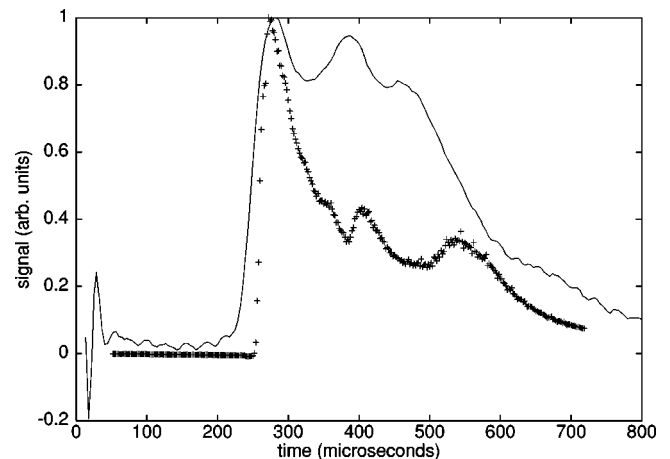


FIG. 5. Detected experimental signal (solid line) for a 10-mW pulse compared to hybrid simulation (+).

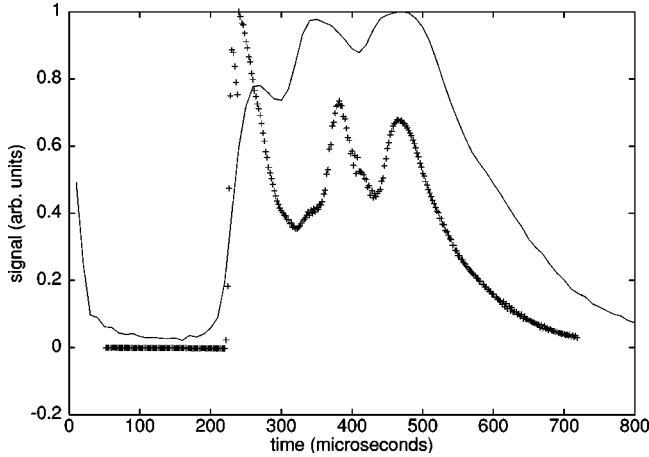


FIG. 6. Detected experimental signal (solid line) for a 16-mW pulse compared to hybrid simulation (+).

ences between successive peaks (as compared to the much shorter pulse creation times) would preclude such an effect. Furthermore, our estimates indicate that only about 10% of the film thickness (which we estimate to be around 30 nm) is evaporated in each pulse.

We considered the possibility that the source heater was warming the film through the λ point and that the singularity of the specific heat at the λ point might account for some of the structure in the detected signals [15]. However, we have included the λ point singularity in the specific heat in our simulation of the temperature of the film (described below in Sec. III and Appendix A) and find that (1) it is very difficult to account for such a large rise in the temperature and (2) even if such a large rise occurred, the λ point singularity would have a very small effect on the detected signal, not at all like what is observed.

Also, by carrying out experiments in which the vapor pulse was detected through a small (75 μm) hole and in which multiple peaks were observed, we eliminated the possibility that the multiple peaks arose from vapor pulses originating at different parts of the apparatus.

The simulations described below indicate that the temperatures and pressures of these pulses are sometimes such that the equilibrium phase is liquid, not gas. Thus, we need to consider the possibility that droplets of liquid could be forming in the pulses. We discuss this in more detail in the last section. Basically, we conclude that there is not enough time in these experiments for the liquid to form, so that the gas phase is kinetically, though not thermodynamically, stable.

III. BOLTZMANN GAS-DYNAMICS SIMULATIONS

To explore the possibility that the pulse shapes arose from dynamics of the vapor, we first carried out gas-dynamics (GD) simulations [16,17] to describe the detected signals observed in pulse experiments. The creation of the pulse was modeled as quantum evaporation of quasiparticles at the surface of the helium as a one-to-one process [14]. The beam creation algorithm is briefly described in Appendix A. It relies on a source temperature simulation developed by Enz

and Lidke [13,18] using an acoustic mismatch model for phonons at the material boundaries of the source and adsorbed helium [19]. Using the time-dependent temperature of the source, the code determines how many particles should be created during each time step and what their velocities should be. The number of particles created each time step is given by

$$N = \frac{1}{4} \rho_0 A \bar{v} \Delta t_0, \quad (1)$$

where Δt_0 is the time step, A is the area of the source, ρ_0 is the vapor density of helium corresponding to the source temperature, and \bar{v} is the mean thermal velocity of the atoms for this temperature. The velocity of the atoms coming off the source are determined from a Maxwell distribution that includes the source temperature. If the energy of the created atom lies between the roton minimum and the maxon, two more particles with velocities that possess the same energy as the original particle are also generated. This is done to account for the quasiparticle dispersion curve for helium, which is triply degenerate in energy between the roton minimum and the maxon, since we assume that the helium atoms are evaporated from the surface via a one-to-one quasiparticle-atom process. Atoms in the pulse collide elastically at rates determined from a cross section calculated from an accurate helium atom interaction potential [20]. (This cross section grows very large when the relative velocity between the atoms is small.)

Since our gas-dynamics simulation can only handle a small number of atoms ($< 10^6$) due to limitations on computer memory and run time, we employ periodic boundary conditions for the gasdynamics simulation in the transverse directions. In order to increase the speed of our scattering algorithm, space in the longitudinal direction is partitioned so that we only need to check an individual atom's partition for collision partners. To further optimize this algorithm, each atom in a partition is tested only to see whether it will collide with any other atom in the partition that is also in its "neighborhood." The "neighborhood" is defined as a spherical space around an atom with a radius that is larger than the maximum velocity in the simulation multiplied by the time step so that relevant collision partners during that time step are not omitted. With a collection of potential collision partners for an atom thus determined, the code then selects one collision partner as follows. First, for each potential collision partner, the distance of closest approach (impact parameter) and the time required to get to closest approach on the present ballistic trajectories is computed. Then all those potential partners for which the time to get to closest approach is longer than the time step are eliminated as candidate partners. Of the remaining potential collision partners (if any), the ones for which the ratio of the collision cross section (found from a realistic form of the helium interatomic potential [21]) to π times the square of the impact parameter s is less than one are eliminated. Finally, of the remaining potential partners, the partner with the largest ratio of the collision cross section to the the square of the impact parameter is selected as the only collision partner. (In practice, it was

quite rare that an atom has more than one potential collision partner for a given time step.) Once the collision partner is known, the velocities of the particles are changed using the relations (see Appendix B)

$$\theta = \cos^{-1}[(2\pi s^2)/\sigma_{total} - 1], \quad (2)$$

$$\vec{v}'_1 = \vec{V} + (\vec{v}_1 - \vec{v}_2)\cos\theta/2 + \hat{i}_\perp|\vec{v}_1 - \vec{v}_2|\sin\theta/2, \quad (3)$$

$$\vec{v}'_2 = \vec{V} - (\vec{v}_1 - \vec{v}_2)\cos\theta/2 + \hat{i}_\perp|\vec{v}_1 - \vec{v}_2|\sin\theta/2, \quad (4)$$

where $\vec{V} = (\vec{v}_1 + \vec{v}_2)/2$ is the center-of-mass velocity of the pair. Here, σ_{total} is the total (energy dependent) cross section in the center-of-mass frame, assumed to be entirely s wave. (The latter is a very good approximation at the energies of interest here.) θ is the angle between $\vec{v}_1 - \vec{v}_2$ and $\vec{v}'_1 - \vec{v}'_2$ and \hat{i}_\perp is a unit vector perpendicular to $\vec{v}_1 - \vec{v}_2$ and in the plane of the vectors $\vec{v}_1 - \vec{v}_2$ and $\vec{v}'_1 - \vec{v}'_2$.

For the lower power pulse densities, we found that the frequency of collisions diminishes so much that the atoms can be treated ballistically after a simulation time corresponding to two to three times that of the pulse creation time. The collisions occur near the source, and each atom, on average, is involved in approximately a hundred scattering events. Three-body collisions are neglected in the runs giving the data reported here. When three-body collisions were included, we found that their effect was negligible. Once the collisions die out, the velocity and temperature distributions for the system are determined, and the time-dependent energy signal at the detector location is calculated. This time-dependent signal is the sum of the kinetic energy for each individual atom in the pulse, plus the energy, $|\mu| = 7.15$ K, given up by the atom when it condenses onto the liquid helium adsorbed on the bolometer.

Applying periodic boundary conditions in the directions normal to the beam propagation direction, we were able to simulate a characteristic portion of the low power experimental helium pulses which are being created in the laboratory by means of computations on about 10^4 helium atoms in pulses created over $1 \mu\text{s}$. (We have done some simulations on up to 10^6 particles.) As time progresses, the collisions die off as the pulse spreads. Thus, at a certain point for these low power pulses, the beam could be treated ballistically as previously mentioned. To make fits to observed beam signals we also took account of effective beam collimation and of some particle losses in the directions normal to the propagation directions. Both the experiments and the simulations showed evidence of local cooling due to two different effects, distinguishable in principle, arising from collisions and from geometrical effects of expansion and collimation. This is consistent as well with previous theories [21,22] and experiments [6,23]. One of these GD calculations is compared with data for a low power pulse in Fig. 3.

IV. HYDRODYNAMIC AND HYBRID SIMULATIONS

Though the low power pulse shapes could be understood by use of this GD model, the higher power pulses involved

much larger numbers of atoms, rendering a GD description infeasible. Except near the interface, where an accurate determination of the boundary conditions requires a microscopic GD description, the length and time scales of this experiment permit a hydrodynamic description of the gas flow. Accordingly, we have used a hydrodynamic model away from the interface. The appropriate hydrodynamic regime is easily determined by estimating the Reynolds number for this flow [24]. At the temperatures in these gas pulses, the sound velocity is less than or of order 100 m/s, which is of the same order as the flow velocity of the pulse relative to the background gas. Accordingly, we estimate [24] that the Reynolds number is $\approx L/l > 10^4$, where $L \approx 1$ cm is the approximate length of the pulse and $l \approx 10^{-4}$ cm is the mean free path. In this regime of Reynolds numbers, the Navier Stokes equations reduce to the Euler equations and are well known [24] to sustain shock waves. For these reasons, we have obtained two codes (originally used for astrophysical calculations) which solve the full nonlinear Euler equations and, in particular, reproduce well known simple shock wave solutions to the Euler equations. The two codes are, respectively, appropriate for one- and for three-dimensional problems. Both codes predict shock wave solutions of the same qualitative type for our application, but we will mainly report results from the three-dimensional code, because we found that the effects of spreading of the pulse during propagation, which obviously cannot be well reproduced in a one-dimensional simulation, are qualitatively significant.

In applying the hydrodynamic equations to this problem, we require an initial condition on the hydrodynamic variables (density, velocity, and temperature) as well as a time-dependent boundary condition as time proceeds to account for the changing temperature and particle emission from the liquid surface. Thermal simulation of the source might be used to estimate the time-dependent temperature, but density and velocity fields require information about the gas dynamics at the interface. Accordingly, we carried out a hybrid calculation, in which the GD code was used in two ways: (1) The GD code was used to determine an initial condition for the hydrodynamic variables $\rho(\vec{r}, t)$, $\vec{v}(\vec{r}, t)$, and $T(\vec{r}, t)$. (2) The GD code was run to determine a time-dependent boundary condition for these variables ‘‘on the fly’’ while the hydrodynamic code was running. We found it useful to carry out the hydrodynamics calculation on two scales, with a finer mesh size used in the earlier part of the simulation when the pulse is near the source and a coarser mesh used later in the hydrodynamic simulation. Initial conditions for the coarser hydrodynamics calculation were determined by averaging values from the finer one.

To validate this method, we first carried out an analysis using a one-dimensional hydrodynamic code [25]. We obtained results for a calculation in which the source was heated by a very short $50\text{-}\mu\text{s}$ current pulse. Figure 7 shows the spatial distribution of density about $40 \mu\text{s}$ after the pulse was ended, calculated in two ways: first using the GD simulation and second in a hybrid code, in which the GD simulation was carried out over a much smaller region near the source and was used to fix the velocity, density, and energy flux boundary conditions for a hydrodynamics simulation

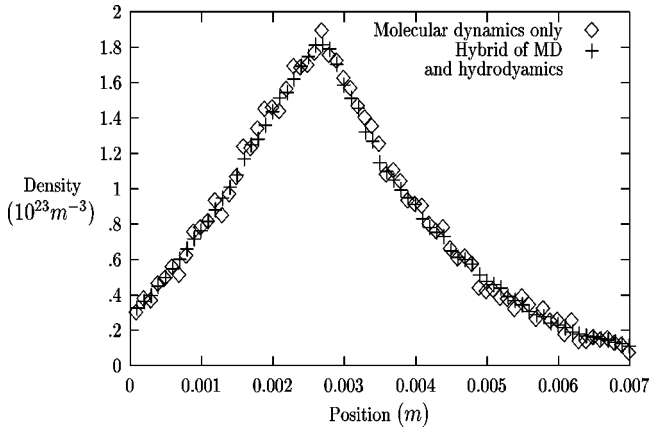


FIG. 7. Comparison of density profiles of the GD and the hybrid simulation using a one-dimension hydrodynamics code.

which treated most of the simulation volume. The hybrid code ran many times faster than the purely GD one and gave equivalent results. (The GD-only code took over a month to run, while the hybrid code required less than a day to reach completion on a 1 GHz processor computer.)

To model the experiments, we used a three-dimensional hydrodynamics code written by the numerical astrophysics group at the University of Virginia [26], which employs a piecewise parabolic method developed by Colella and Woodward [27]. A three-dimensional code turned out to be necessary because the escape of particles from the beam in directions parallel to the source was significant. But this raised the problem of taking account of this transverse direction in matching the GD calculation, carried out with periodic boundary conditions in the transverse direction, to the hydrodynamic one. (A GD simulation with a realistic finite size in this transverse direction would be totally impractical since the large number of atoms required would be computationally impossible to model.)

In order to determine an initial condition for the density and velocity profiles of the hydrodynamic regime at all points in space, we used a profile in the transverse direction (parallel to the source surface) which was obtained from a ballistic model for the pulse propagation. This use of a ballistic model for setting the transverse boundary conditions is forced on us by the limitations of the gas dynamics and constitutes one of the major sources of uncertainty in the calculation. It can be partially justified by noting that there is only a very narrow collision region near the source in the gas pulses. However, we discuss this further in the last section and present results of varying features of this assumption there. Details of the ballistic model are described in Appendix C. From this ballistic model, we obtain an envelope function $E_{\rho,ball}(r,z,t)$. The initial and boundary values of the density of the pulse are then obtained from the GD simulation by the relation

$$\rho_{pulse}(r,z,t) = \rho_{GD}(z,t) \times E_{\rho,ball}(r,z,t). \quad (5)$$

Here, $\rho_{GD}(z,t)$ is the result of the gas-dynamic simulation, which depends only on time and on the coordinate z in the direction perpendicular to the source surface, because the

gasdynamic simulation is periodic in the two dimensions parallel to the source. $E_{\rho,ball}(r,z,t)$ is the envelope function, which is determined from a ballistic model. It is defined to be the ratio of the value of the density in the ballistic model at (cylindrical coordinate) r to the value of the density in the ballistic model at $r=0$ as explained in Appendix C. Since there is also a stationary background gas in the experiment, the total density at any point is given by

$$\rho(\vec{r},t) = \rho_{pulse}(\vec{r},t) + \rho_{bkgd}(\vec{r}). \quad (6)$$

The values of $\rho(\vec{r},t)$ as determined from the one-dimensional gasdynamics simulation, the ballistic model, and the last two equations are then used to determine initial and boundary conditions for the density in the hydrodynamic calculation. The initial and boundary conditions for the transverse components of the hydrodynamic velocities are found in a similar fashion from the ballistic model as described in Appendix C. The biggest problem was to determine a satisfactory initial condition on the hydrodynamic velocity in the direction normal to the source surface. This was difficult because the GD calculation could not be carried out in a way which took account of a background gas that causes the hydrodynamic velocity to go to zero at large distances from the surface. Furthermore, the results were very sensitive to this initial condition on the velocity function. Ultimately, we used a rather simple and physically sensible initial condition. First, we find a hydrodynamic pulse velocity $v_{pulse}(z,t)$ from the GD simulation. Then the initial and boundary values $v_z(r,z,t)$ of the hydrodynamic velocity are given by the relation

$$v_z(r,z,t) = \left[\frac{\rho_{pulse}(\vec{r}) \vec{v}_{pulse}(z,t)}{\rho(\vec{r})} \right]. \quad (7)$$

This relation gives an initial condition on the velocity which results in the same particle current as the pulse simulation and which goes to zero as it should at large z for the stationary background gas. We also used this relation, the ballistic model for the transverse velocities (Appendix C) and Eq. (6) for the time-dependent boundary conditions during the hybrid calculations as described below, although in fact the GD-hydrodynamic interface is very close to the circular source ($\approx 20 \mu\text{m}$ compared to a 1 mm source radius) so that the dynamic boundary conditions could have been treated uniformly across the area of the source on the hydrodynamic grid. We actually found that inclusion of a time-dependent envelope function at the GD-hydrodynamic interface where the source is located, had very little effect on resultant pulse shapes.

The addition of the background gas $\rho_{bkgd}(z,0)$ turned out to be very important physically. In the experiments, the detector was at a higher temperature (about 0.47 K) than the source and ambient temperature (about 0.3 K), resulting, in local equilibrium, in a positive density gradient from source to detector. The shock waves which are observed in the experiment are only reproduced in the model if this density gradient in the ambient background is present. Thus, we can interpret the physical phenomenon causing the multiple

peaks as the generation of shock waves in the vapor arising from the incident vapor pulse colliding with the density gradient of the ambient background gas.

After the hydrodynamic code is initialized, the hydrodynamic and GD simulations run in tandem. This initialization of the hybrid code occurs 10 μs into the generation of the 50- μs pulse. This insures that we have done enough statistical averaging of the hydrodynamic quantities from the GD simulation when it is replaced, on the hydrodynamic side of the GD-hydrodynamic interface, by the hydrodynamic simulation. The time step for the hydrodynamics code is determined by the Courant constraint

$$\Delta t = \min(\Delta z/v, \Delta z/c_s), \quad (8)$$

where Δz is the size of the spatial mesh, v is the hydrodynamic velocity at that mesh point, and c_s is the corresponding sound velocity at that mesh point. The hydrodynamic time step is compared to the GD time step to determine the next time the hydrodynamic algorithm is to be called.

The boundary conditions at the source for successive hydrodynamics time steps are determined from the GD part of the simulation, while the boundary conditions in the transverse directions are assumed to be open. The hydrodynamic quantities for the first grid points for successive time steps are given by

$$\rho_1^{next} = \rho_1 + \frac{\Delta t}{2\Delta z}(\rho_{gd}v_{gd} - \rho_2v_2), \quad (9)$$

$$(\rho_1v_1)^{next} = \rho_1v_1 + \frac{\Delta t}{2\Delta z}(\rho_{gd}v_{gd}^2 + p_{gd} - \rho_2v_2^2 - p_2), \quad (10)$$

$$E_1^{next} = E_1 + \frac{\Delta t}{2\Delta z}[(E_{gd} + p_{gd})v_{gd} - (E_2 + p_2)v_2]. \quad (11)$$

Here, the subscript *gd* means that the quantity was determined from the gasdynamics simulation with the corrections for transverse variation using a ballistic model as described above. The subscripts 1 and 2 refer to the first two grid points of the hydrodynamics (right) zone. The superscript *next* refers to the values to be used in the next hydrodynamic time step, ρ is the mass density, v is the velocity, p is the pressure, and E is the energy density. Since we are modeling a finite beam source in the experiment, the boundary condition for the grid points at the GD-hydrodynamics interface that lie outside of this source are assumed to be open.

Because there may be backward moving particles in the simulation, we have to take into account particles that traveled back from the hydrodynamics zone into the zone treated by the GD simulation. Because the GD zone is extremely narrow compared to the source radius, the flux of particles between the zones is nearly uniform throughout the area of the source. Therefore, since this backward flux is nearly radially independent at the GD-hydrodynamic interface, no treatment of this radial dependence, which becomes rather important far from the source, is required in the part of the algorithm which returns particles from the hydrodynamic

side to the GD side of the simulation (though this could be done). The distribution of the particles, being Boltzmann like about a center of mass velocity with a temperature corresponding to that at the interface, can be used to determine the number of atoms that have negative velocities and, thus, would cross back into the GD zone. At each hydrodynamic time step, the probability of adding a particle for a given GD time step is calculated, and atoms with velocities calculated from this Boltzmann distribution are returned to the GD side of the simulation.

After the hybrid code runs until the moving pulse begins to affect the hydrodynamic variables at the far right boundary, the hydrodynamic code is rescaled in order to simulate the correct source-to-detector distance of the experiment. Modeling of this distance is inaccessible initially due to limitations on the size of the hydrodynamic arrays within our code. Although the mesh distances could be chosen to be larger when first invoking the hydrodynamic simulation, they are made small to capture the effects of fluctuations in the GD simulation.

Once the pulse is entirely created, the boundary at the source is made open since there is very little net flux of particles across the GD or hydrodynamics interface. At this point, the GD code is turned off and the pulse is treated solely by the hydrodynamics simulation. Further rescaling is also done long after pulse creation in order to increase the simulation's run time. It is found that this rescaling had very little effect on the resultant signal and, therefore, was justified. The signal itself is also determined during this last step in the simulation. The energy flux at the right boundary, where the detector is located, is integrated over the area of the detector to determine the pulse's signal. Once times corresponding to the completion of a pulse's propagation in the experiments are reached, the code exits.

We show calculated profiles of the detected signals obtained with our hybrid code, varying only the source power, in Figs. 4–6. These profiles were generated by averaging the individual profiles of a number of simulation runs in which the random number generator in the code was seeded with different values. Averaging over approximately ten runs for each profile was sufficient so that averaging in additional runs altered the resultant profile only slightly. In all these figures, we have adjusted an overall scale in both the experimental and the calculational data so that the largest peak height in each dataset is 1. Thus, the overall amplitudes in these comparisons are not significant. However, we do find that our calculations give signals at high powers which are many orders of magnitude larger than those at lower powers, in qualitative agreement with the experiments.

The time-dependent voltage placed across the source was used to find the temperature dependence of the source and corresponds to that used in the experiments. The initial background vapor density gradient, which is determined from the temperature of the bolometer detector, was kept constant for each of the simulations. As the source power was systematically increased, the simulated detected signal evolved from one to two and finally to three peaks with peak times and amplitudes similar to those from the experiments, also shown in Figs. 4–6. The peak positions are quite well reproduced,

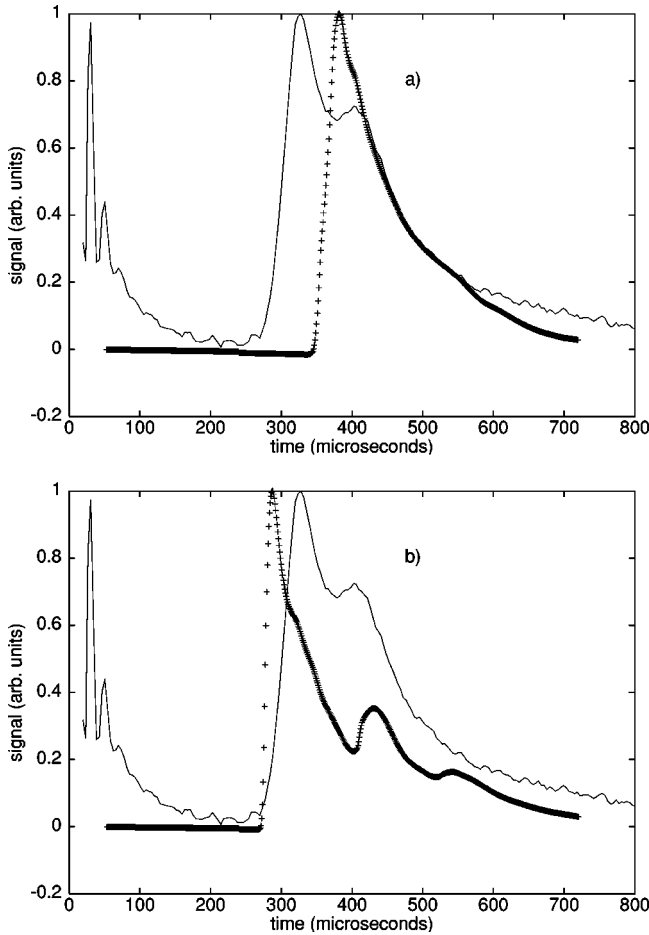


FIG. 8. Results for a 4-mW pulse with a narrowed (a) and broadened (b) transverse envelope (+) compared to experiment (solid line).

but the calculated leading peak is sharper than the experimentally observed one for the higher power pulses.

V. DISCUSSION AND CONCLUSIONS

Though both the detected and calculated signals are quite complex, particularly at the higher powers, we have a qualitative understanding of the nature of at least the three large peaks, as seen, for example, in Figs. 5 and 6: We attribute the last of the three peaks to a remanent of the pulse which occurs in the absence of shock waves arising in the presence of a background gas density and/or at low powers (as seen, for example, in Fig. 3). One indication of this is that the propagation time for this peak (between 400 and 600 ms) remains approximately the same as the power is increased. The other two, earlier, peaks are the result of the shock waves that occur when the pulse encounters the background gas density gradient. (Such a shock results in two waves, in advance and behind the initial discontinuity [24].) We think of the earliest peak as the result of gas density piling up as the pulse hits the background gas density and the peak at intermediate times as the result of a wave recoiling behind the shock resulting from this impact.

It is clear that, although in Figs. 4–6 the calculated peak

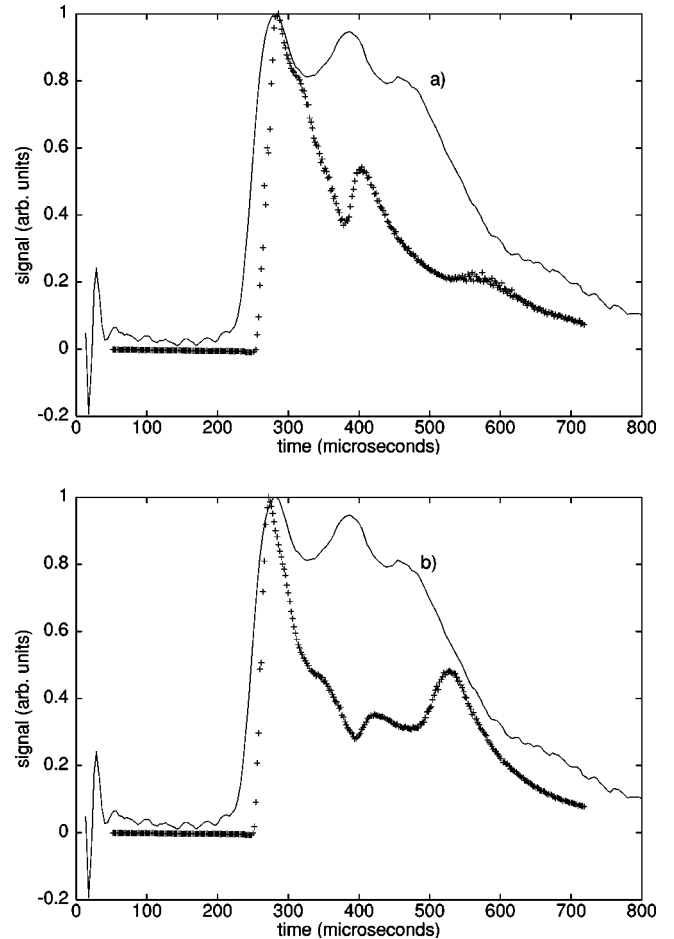


FIG. 9. Results for a 10-mW pulse with a narrowed (a) and broadened (b) transverse envelope (+) compared to experiment (solid line).

positions are quite well reproduced by our calculations, the relative peak amplitudes are not, particularly at 10 mW (Fig. 5). We have explored the extent to which these discrepancies might be understood as arising from two uncertainties in the calculations, namely, (1) the use of a ballistic model to complement the gas dynamics and supply a transverse envelope for the initial and boundary values of the density and for the initial and boundary values for the transverse velocity and (2) uncertainties in the background ambient density. We next briefly discuss these two possible origins of the discrepancies. In Figs. 8–10, we show results of recalculation of the calculated signal when the envelope function is recalculated with ballistic envelopes which are narrower and broader than the ones calculated from the model described in Appendix C for the three different pulse powers. (In practice, for example, the data in Fig. 10 was generated by computing the envelope function $E_{p,ball}(r,z,t)$ as well as the transverse velocity distribution of Appendix C, but not $\rho_{GD}(z,t)$, as if the power were, respectively, 9.6 mW and 25.6 mW, while $\rho_{GD}(z,t)$ was still calculated assuming that the source power was 16 mW.) One sees from the results in Figs. 8–10, that the width of the ballistic model envelope has quite a big effect on the peak positions. These changes in the envelope function are quite small and these and similar results we

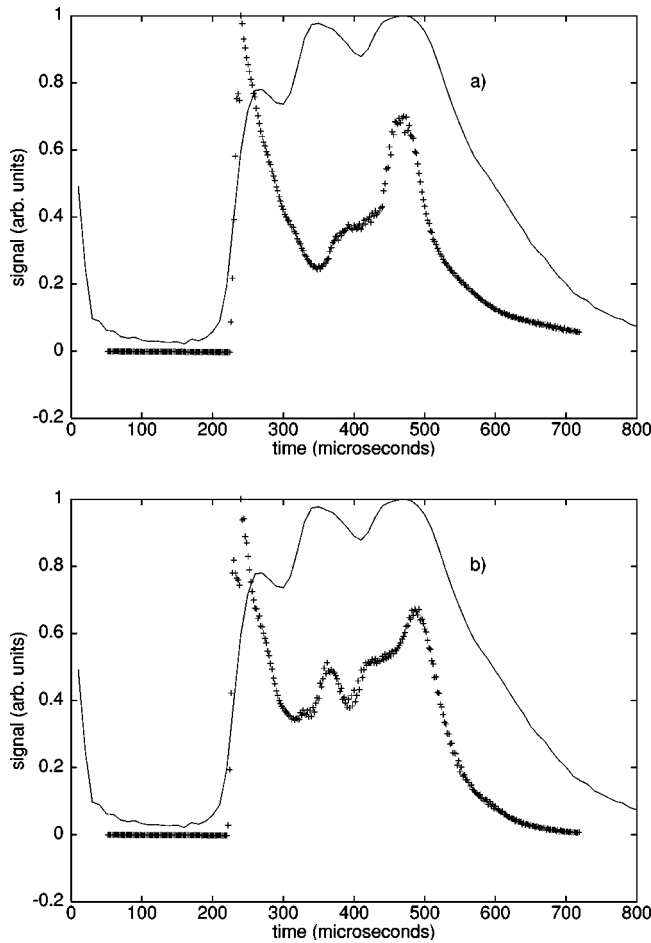


FIG. 10. Results for a 16-mW pulse with a narrowed (a) and broadened (b) transverse envelope (+) compared to experiment (solid line).

have obtained indicate a strong sensitivity of the model to the assumptions about the transverse dependencies. However, the data in Figs. 8–10 agree less well with the experimental data than those in Figs. 4–6 which was based on our attempt to use the most realistic ballistic model possible for the transverse dependencies. We conclude that, though the model is sensitive to the transverse dependencies in the initial and boundary conditions, it is not very likely that the discrepancies between the model and experiment are mainly due to inaccuracies arising from our assumption of a ballistic model to estimate these dependencies.

To explore the effects of the background gas on the simulation, we made several calculations in which the background gas density was varied. For example, in Figs. 11–13 we compare results with the 4-, 10-, and 16 mW pulses, of lowering and raising the background gas density by 40% with experiment. Characteristically, these data show that the first, early time peak is especially sensitive to the background gas, consistent with our qualitative interpretation that this peak arises because the incident gas pushes a shock wave of background gas in front of it. It does appear that the observed pulse shapes could be fit somewhat better to the simulations by regarding the background density gradient as a fitting parameter. However, no general conclusions can be

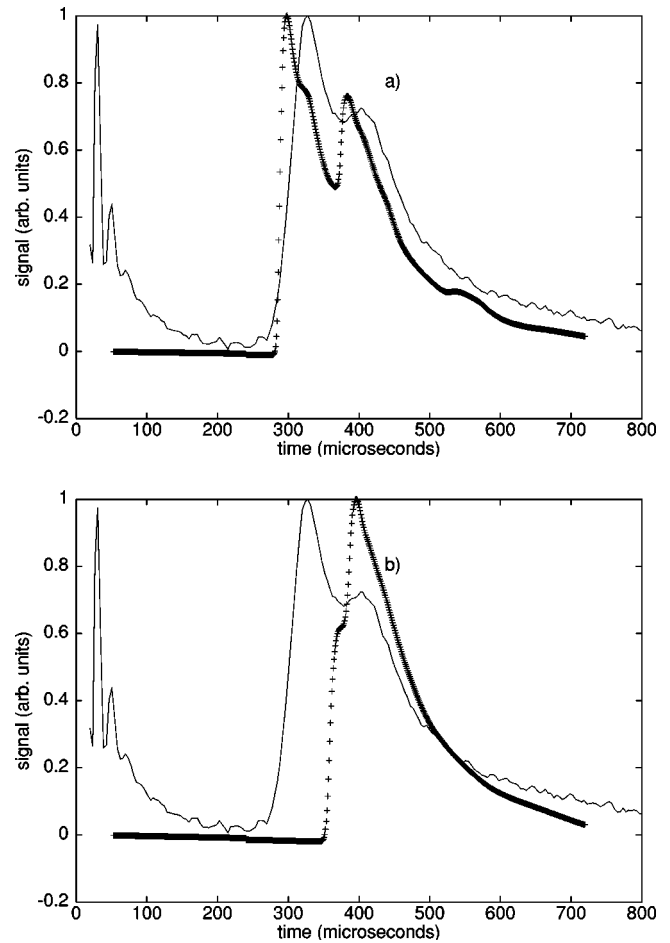


FIG. 11. Effect of varying background gas density for the 4-mW pulse (+) as compared to experiment (solid line). (a) shows the effect of decreasing the gradient of the density ramp and (b) shows the effect of increasing the gradient of the density ramp.

drawn because the lowest power pulse appears to require an increase in background density in such an approach, whereas the higher power pulses are better fit with a reduced density gradient. However, bearing in mind that the peak heights are normalized to 1 at the largest peak height in all these comparisons and also the qualitative interpretation of the three major peaks as discussed at the beginning of this section, we can understand many of the qualitative features of the results in Figs. 11–13: Increasing the density gradient increases the relative magnitude of the leading peak, which then, in extreme cases, can mask profile of the original pulse so that it is invisible [as in Fig. 11(b)] or significantly reduced in relative magnitude [as in Figs. 12(b) and 13(b)]. At steeper gradients the leading pulse position is delayed in time. This effect is larger when the power is low (Fig. 11) than at higher powers.

We note that the intermediate, nominally 10 mW signals were in the least satisfactory agreement with the simulations and we have explored the possibility that this could be because the experimental power was in fact somewhat higher than that used in the calculation. For example, we show a simulation with a power of 11 mW and the enhanced gradient (40% larger than estimated) compared with the nomi-

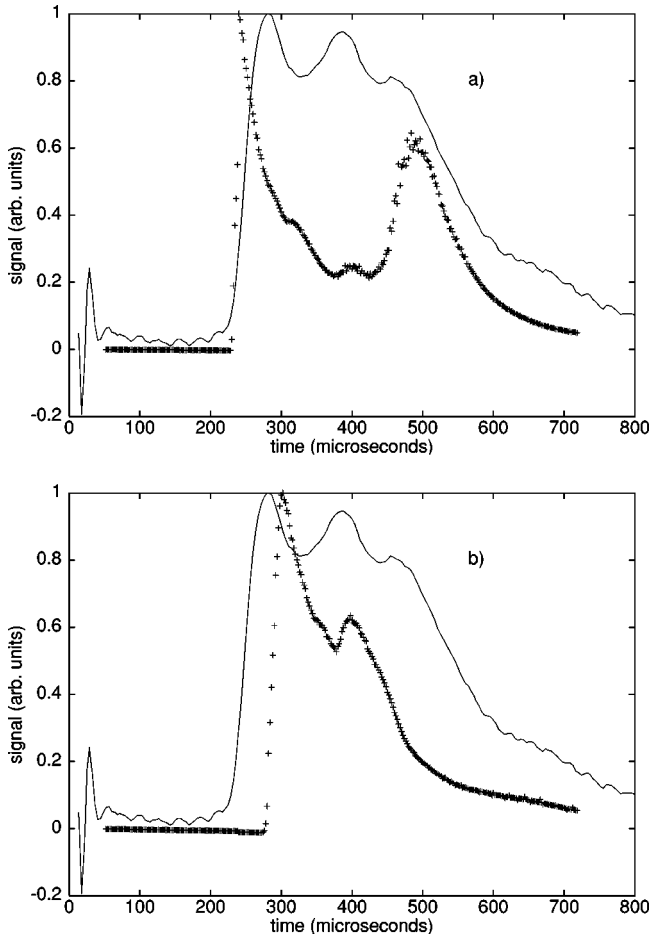


FIG. 12. Effect of varying background gas density for the 10-mW pulse (+) as compared to experiment (solid line). (a) shows the effect of decreasing the gradient of the density ramp and (b) shows the effect of increasing the gradient of the density ramp.

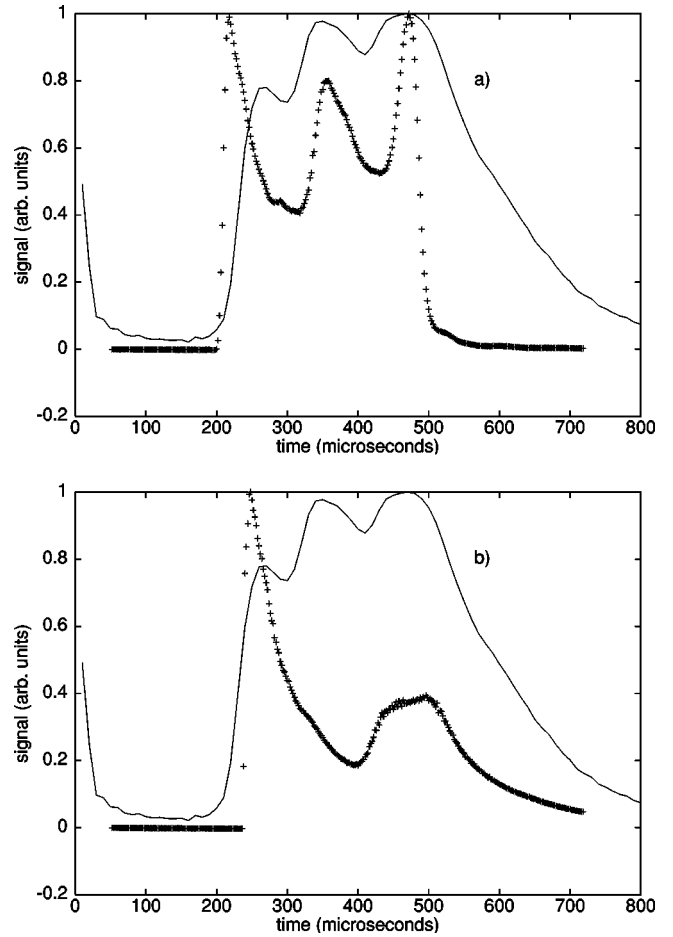


FIG. 13. Effect of varying background gas density for the 16-mW pulse (+) as compared to experiment (solid line). (a) shows the effect of decreasing the gradient of the density ramp and (b) shows the effect of increasing the gradient of the density ramp.

nally 10 mW data in Fig. 14. The calculated profile is in better agreement with the experiment than that shown in Fig. 5, indicating that the 10 mW data could be fit better if the power and gradient were used as fitting parameters. However, we do not engage in any further such curve fitting exercises here.

With regard to the possibility of liquid droplet formation in these pulses, we have estimated the range of kinetic stability of the vapor phase in these experiments as follows: The rate of liquid formation is limited by the rate of three-body collisions per particle which is in turn expected to be proportional to the square of the vapor density times the thermal velocity $1/\tau_3 \approx a^5 \rho^2 v$, where a is a length characterizing the size of the atoms and v is the thermal velocity. One estimates that liquid cannot form as long as the time of the experiment t_{expt} is shorter than τ_3 which, with the above estimate for τ_3 and the ideal gas law gives $P < (m/k_B)^{1/4} (k_B/a^{5/2}) [T^{3/4}/t_{expt}^{1/2}]$ or, rearranging $P < (a/v)^{1/2} (1/t_{expt})^{1/2} (k_B T/a^3)$. In pulsed experiments, we may estimate t_{expt} as the time at which collisions stop, which is of order $t_{expt} \approx 1/\rho v a^2$ so that, using the ideal gas law again the requirement is $P < k_B T/a^3$. (All factors of order one have been dropped.) This is quite plausible and gives an

estimated value of around 10^4 Pa/K or 75 torr/K for the ratio $A = P/T$. Assuming that this kinetic stability line is of the form $P = AT$, as implied by this argument, we have also estimated the coefficient A in another way for the lowest

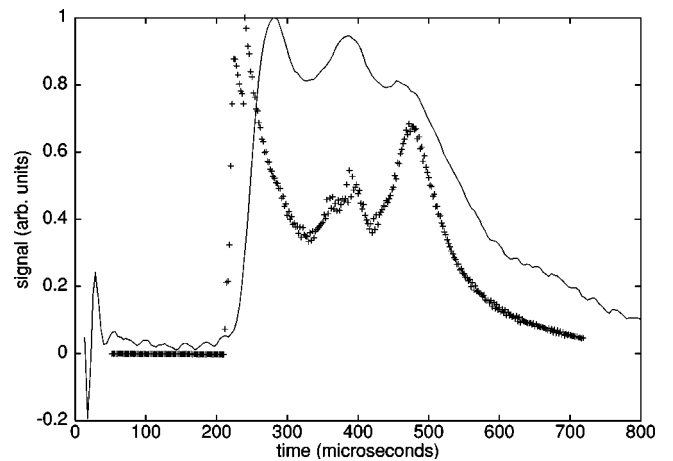


FIG. 14. Simulation results with 11-mW power and a reduced density gradient compared with the experimental data at 10 mW.

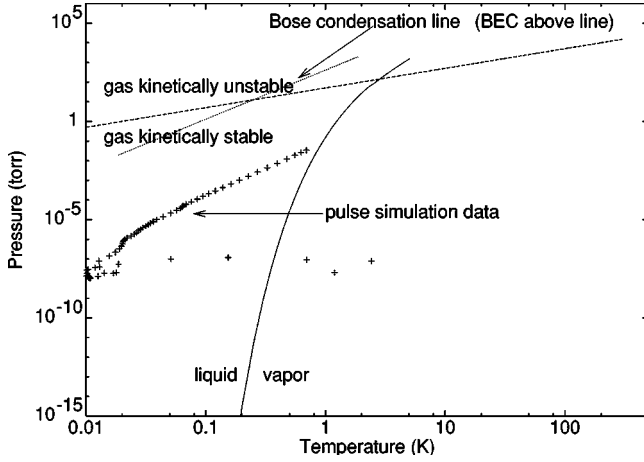


FIG. 15. Regions of thermodynamic and kinetic vapor stability together with locus of pressure and temperature found in a high power simulated pulse. A line of Bose-Einstein condensation transitions is also shown.

initial pressure for creating dimers. The value of A is found to be 7000 Pa/K or 50 torr/K. These values are in good order of magnitude agreement. In Fig. 15, we show these estimates (using the second, experimentally based, value of A) together with the locus of pressures and temperatures within a simulated pulse. One sees that, while the vapor in the pulse has temperatures and pressures well within the region of thermodynamic stability of the liquid, the simulated vapor pulse lies well within our estimate of the region of kinetic stability of the vapor. For reference, we also show the region of vapor Bose-Einstein condensation in this figure. There does appear to be a region of kinetic vapor stability in which Bose-Einstein condensation would occur, but the simulated pulse has pressures and temperatures that lie outside it.

With the insights provided by these simulations, we have been able to improve our control of peak shapes and the shock phenomena in our experiments. For example, we have recently essentially eliminated the multiple shock phenomenon by using a detecting bolometer with an operating temperature very close to that of the ambient gas.

We believe that the analysis which led to these conclusions has involved the development of simulation techniques which may have a wider use and significance. Through hybridization of gasdynamics and hydrodynamics, we have not only been able to drastically increase the speed of pulse simulations, but we have also been able to explore experimental regimes that were inaccessible using gasdynamics alone. A background gas in the experiment, which could not be viably modeled in the GD code, could easily be changed and tested in our hybrid model. And since the time needed to complete a simulation, which requires less than a day with our hybrid model as compared to months using GD alone for even the lowest power pulses, has been greatly reduced, we have been able to change parameters quickly and observe their effect on a signal without having to wait weeks for previous simulations to finish.

ACKNOWLEDGMENTS

This work was supported by NASA, by NSF Grant No. NSF/DMR 9980329, and by the Physics Department, the

Graduate School, the Institute of Technology, and the Supercomputing Institute of the University of Minnesota. We thank Sarah Alfano for writing a preliminary version of the gasdynamics code. William Zimmermann is thanked for sharing facilities in the laboratory and for numerous discussions. Thomas Jones is thanked for assistance with hydrodynamics codes.

APPENDIX A: SOURCE TEMPERATURE SIMULATION

The time-dependent temperature of the evaporating helium on the beam source is found by numerically integrating the following coupled equations:

$$C_1 \frac{dT_1}{dt} = \frac{A_{12}}{k_{12}}(T_2^4 - T_1^4) + \frac{A_{13}}{k_{13}}(T_3^5 - T_1^5) - P_{evap},$$

$$C_2 \frac{dT_2}{dt} = \frac{A_{12}}{k_{12}}(T_1^4 - T_2^4) + \frac{A_{23}}{k_{23}}(T_3^4 - T_2^4) + P_{bias} - P_{leads}, \quad (A1)$$

$$C_3 \frac{dT_3}{dt} = \frac{A_{13}}{k_{13}}(T_1^5 - T_3^5) + \frac{A_{23}}{k_{23}}(T_2^4 - T_3^4),$$

where the subscripts refer to the adsorbed helium film (1), the chromium metal film (2), and the sapphire substrate (3). A corresponds to the boundary area between these materials and k is the kapitza resistance (or thermal boundary resistance) between the materials. The voltage pulse applied across the source heats the metal film, P_{bias} . Heat is carried away from the source by evaporated particles P_{evap} and conduction along the support wires and electrical leads, P_{leads} . The voltage pulse applied across the source heats the metal film via joule heating

$$P_{bias} = I^2 R_{source}. \quad (A2)$$

The helium film is cooled by energy carried away by evaporated particles. The rate of energy transfer is found by taking the rate of particle evaporation multiplied by the average energy removed per particle, which consists of the average kinetic energy per particle plus the magnitude of the chemical potential of an atom in the adsorbed film, giving

$$P_{evap} = \frac{1}{4} n_{vap}(T_1) \bar{v} A_1 (|\mu| + 2k_B T_1), \quad (A3)$$

where A_1 is the area of the source and the vapor pressure of helium at temperature T is given by

$$n_{vap}(T) = \frac{(2\pi m)^{3/2}}{h^3} (k_B T)^{3/2} \exp\left(\frac{-|\mu|}{k_B T}\right), \quad (A4)$$

the thermal velocity is $\bar{v} = \sqrt{8k_B T / \pi m}$ and μ is the chemical potential of the liquid. Heat conduction along the support wires and electrical leads gives a heat flow out of the source

$$P_{leads} = \sum_i \frac{A_i}{L_i} \int_{T_0}^{T_2} k_i(T_1) dT_1, \quad (A5)$$

where T_0 is the cell temperature, i represents each lead, and A , L , and k are the cross sectional area, length, and thermal conductivity, respectively, of each lead.

APPENDIX B: COLLISION ALGORITHM

We use the classical definition of the cross section [28] for which

$$2\pi s' ds' = -2\pi(d\sigma/d\Omega)\sin\theta' d\theta'.$$

Integrating s' from 0 to s and θ' from π to θ gives Eq. (2) in the center of mass frame, where $\sigma_{total} = \int d\Omega d\sigma/d\Omega$. In the laboratory frame the velocities of the incident particles are

$$\vec{v}_{1,2} = \vec{V} \pm \vec{v}/2$$

in which the center of mass velocity \vec{V} is conserved during the collision as well as the modulus of $\vec{v} = \vec{v}_1 - \vec{v}_2$. These results lead to Eqs. (3) and (4). In this classical approximation to the scattering we are obviously neglecting interference effects, but we include the known energy dependence of the total cross section.

APPENDIX C: BALLISTIC MODEL

The number of particles that are emitted from the source per unit time t_0 is given by

$$\frac{dN}{dt_0} = \frac{1}{4} \rho_0 A \bar{v}, \quad (C1)$$

where the vapor density ρ_0 and the thermal velocity $\bar{v} = \sqrt{8k_B T/\pi m}$ depend on the time-dependent temperature of the source. The number in a given velocity range \vec{v} and $\vec{v} + d\vec{v}$ emitted per unit time is given by the function

$$\frac{dN}{dt_0} \frac{m^2}{2\pi(k_B T)^2} v_z \exp\left(-\frac{mv^2}{2k_B T}\right) d\vec{v}, \quad (C2)$$

since the generated atoms have a Maxwell-Boltzmann velocity distribution. The velocities, in turn, can be written as

$$\vec{v} = \frac{\vec{r} - \vec{r}_0}{t - t_0}, \quad (C3)$$

where t_0 and \vec{r}_0 are the time and location of the particle's creation, and t and \vec{r} are the time and location of the particle sometime later. Likewise, the differential element $d\vec{v}$ can be replaced with

$$d\vec{v} = \frac{d\vec{r}}{(t - t_0)^3}, \quad (C4)$$

so that the density per unit time due to particles created at the source at point \vec{r}_0 and time t_0 is

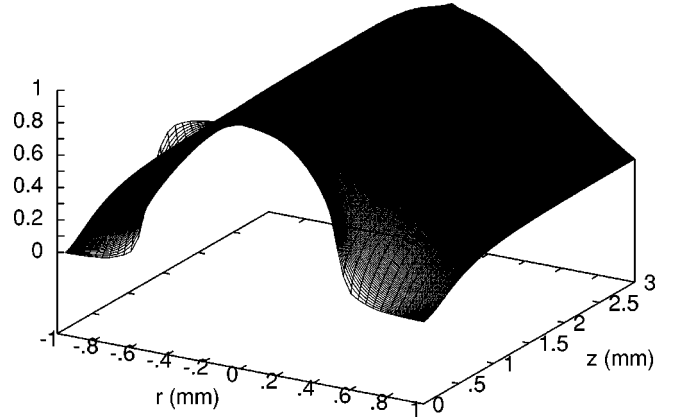


FIG. 16. The envelope function $E_{\rho,ball}(r,z,t)$ for a 16-mW pulse.

$$\frac{dN}{dt_0} \frac{m^2}{2\pi(k_B T)^2} \frac{v_z \exp\left(-\frac{mv^2}{2k_B T}\right)}{(t - t_0)^3}. \quad (C5)$$

Using Eqs. (C1)–(C4), and considering the cylindrical symmetry of the system being modeled, the density at (z,r) at time t is

$$\begin{aligned} \rho_{ball}(r,z,t) = & \int_0^t \int_0^R \int_0^{2\pi} \frac{m^2}{4} \frac{v_z \exp\left(-\frac{mv^2}{2k_B T}\right)}{(t - t_0)^4} \\ & \times \exp\left[-\frac{m^2}{2k_B T} \left(\frac{z^2 + r^2 + r_0^2 - 2rr_0 \cos(\phi_0)}{(t - t_0)^2}\right)\right] \\ & \times r_0 d\phi_0 dr_0 dt_0, \end{aligned} \quad (C6)$$

where R is the radius of the source.

We are using this ballistic model only to obtain an envelope function which gives the transverse r dependence for the initial and boundary values of the hydrodynamic variables. The needed envelope function $E_{\rho,ball}(r,z,t)$ for the density is obtained by normalizing the preceding function so that it is 1 at $r=0$: $E_{\rho,ball}(r,z,t) = \rho_{ball}(r,z,t)/\rho_{ball}(0,z,t)$. We show the resulting envelope function $E_{\rho,ball}(r,z,t)$ at the time at which the hydrodynamic part of the calculation began in Fig. 16.

The transverse velocities at all points at time t are found in a similar fashion by determining their expectation value in Eq. (C6), that is we take

$$\begin{aligned} v_{r,ball}(r,z,t) = & \int_0^t \int_0^R \int_0^{2\pi} (r - r_0) \frac{1}{4} \frac{m^2}{2\pi(k_B T)^2} \rho_0 \bar{v} \frac{z}{(t - t_0)^5} \\ & \times \exp\left[-\frac{m^2}{2k_B T} \left(\frac{z^2 + r^2 + r_0^2 - 2rr_0 \cos(\phi_0)}{(t - t_0)^2}\right)\right] \\ & \times r_0 \cos \phi_0 d\phi_0 dr_0 dt_0. \end{aligned} \quad (C7)$$

- [1] J.W. Halley, C.E. Campbell, C.F. Giese, and K. Goetz, *Phys. Rev. Lett.* **71**, 2429 (1993).
- [2] A. Setty, J.W. Halley, and C.E. Campbell, *Phys. Rev. Lett.* **79**, 3930 (1997).
- [3] J. Harms and J.P. Toennies, *Phys. Rev. Lett.* **83**, 344 (1999).
- [4] E.S. Meyer, J.C. Mester, M.W. Reynolds, T.E. Huber, Z. Zhao, B. Freedman, J. Kim, and I.F. Silvera, *Physica B* **194-196**, 885 (1994).
- [5] J.C. Mester, E.S. Meyer, M.W. Reynolds, T.E. Huber, Z. Zhao, B. Freedman, J. Kim, and I.F. Silvera, *Phys. Rev. Lett.* **71**, 1343 (1993).
- [6] N. Mulders and A.F.G. Wyatt, *Physica B* **194-196**, 539 (1994).
- [7] N. Mulders (private communication).
- [8] C.J. Mundy, S. Balasubramanian, and M.L. Klein, *J. Chem. Phys.* **105**, 3211 (1996).
- [9] C.J. Mundy, S. Balasubramanian, and M.L. Klein, *Physica A* **240**, 305 (1997).
- [10] L. Bocquet and J.-L. Barrat, *Phys. Rev. E* **49**, 3079 (1994).
- [11] R.A. Sherlock and A.F.G. Wyatt, *J. Phys. E: Sci. Instrum.* **16**, 673 (1983).
- [12] C.G.B. Baker and A.F.G. Wyatt, *J. Phys. E: Sci. Instrum.* **20**, 1461 (1987).
- [13] M.J. Enz, Senior thesis, University of Minnesota, 1999.
- [14] M.W. Cole, *Phys. Rev. Lett.* **28**, 1622 (1972).
- [15] J. Hietala, Senior thesis, University of Minnesota, 2000.
- [16] H.H. Hjort, S.A. Viznyuk, and D.O. Edwards, *J. Low Temp. Phys.* **116**, 99 (1999).
- [17] K.A. Lidke, M.C. Williams, A. Wynveen, and J.W. Halley, *J. Low Temp. Phys.* **121**, 351 (2000).
- [18] K.A. Lidke, Graduate Oral Exam Paper (1997).
- [19] A.F.G. Wyatt, *Phys. Rev. Lett.* **69**, 1785 (1992).
- [20] R.A. Aziz and M.J. Slaman, *Metrologia* **27**, 211 (1990).
- [21] G.A. Bird, *Molecular Gas Dynamics* (Clarendon Press, Oxford, 1976).
- [22] J.P. Toennies and K. Winkelmann, *J. Chem. Phys.* **66**, 3965 (1977).
- [23] E.S. Meyer, J.C. Mester, and I.F. Silvera *Phys. Rev. Lett.* **70**, 908 (1993).
- [24] L.D. Landau and E.M. Lifshitz, *Fluid Physics* (Addison-Wesley, Reading, MA, 1959), Chap. IX, pp. 310–346.
- [25] A one-dimensional TVD hydrodynamic code was provided by Tom Jones and written by Dongsu Ryu.
- [26] <http://wonka.physics.ncsu.edu/pub/VH-1/>
- [27] P. Colella and P.R. Woodward, *J. Comput. Phys.* **54**, 174 (1984).
- [28] H. Goldstein, *Classical Mechanics* (Addison-Wesley, Reading, MA, 1959), p. 82.